Machine Learning-Driven State Selection Method for Millimeter-Wave Reconfigurable Array Antenna with 360° Beam Scanning

Md Shakir Hossain, Kyei Anim, Kapil R. Dandekar, *Senior Member, IEEE*

Electrical and Computer Engineering (Email: {mh3696, ak4259, dandekar}@drexel.edu),

Drexel University, Philadelphia, PA 19104, USA

Abstract—Reconfigurable antennas can enhance 5G network coverage and capacity by dynamically adapting their characteristics to overcome propagation challenges in millimeter-wave (mmWave) environments. In this paper, we first present a single-fed cylindrical conformal antenna with beam-steering capabilities to support full 360° azimuthal scanning. The antenna has eight cascading 4×2 subarrays (*i.e.*, a 4×16 array) operating at 28 GHz and is fed by a reconfigurable feeding network, which enables electrical switching between the subarrays to generate eight distinct radiation beams (states). The switching mechanism is implemented through the integration of PIN diodes within the antenna's feeding network, modeled as a lumped RLC boundary in the full-wave simulation. Next, machine learning (ML) techniques are integrated into the state-selection optimization method based on the simulation data to select or predict the optimal beam that enhances network performance. We developed a low-complexity, fast-converging state-selection algorithm suitable for real-time applications and capable of adapting to dynamic environments. Using ray-tracing simulations, we modeled a single-user, single radio frequency (RF) chain mmWave communication system, where only one antenna state can transmit at a time. The received power at each antenna state was then used as the reward metric for the state-selection algorithm.

Index Terms—Reconfigurable Antenna, mmWave Communications, State Selection, Beam Steering, Machine Learning, Adaptive Pursuit

I. INTRODUCTION

Millimeter-wave (mmWave) 5G network technology promises data rates up to 10 times higher than today's 4G LTE networks [1]. The mmWave spectrum provides a practical solution to achieve multi-Gbps data rates, addressing the increasing demand for high-speed internet access [2]. However, the real-world performance of 5G has not fully met these expectations. 5G networks face limited coverage due to their susceptibility to path loss and environmental sensitivity [3]. To bridge the gap between the potential of 5G and its current limitations, advanced antenna systems with reconfigurability, beamforming capabilities, and machine learning (ML) control algorithms are envisioned to play a critical role in increasing 5G network capacity and coverage [4, 5].

Pattern reconfigurable antennas (PRAs) can dynamically reshape their radiation characteristics, allowing precise localization and tracking and enabling 5G antenna systems to adapt to varying physical link conditions in real-time based on the wireless network's needs [6–8]. As a result, reconfigurable
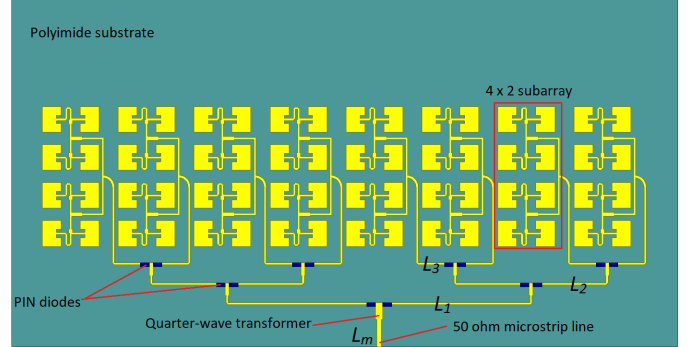

Fig. 1: Geometry of the 4×16 planar array antenna in Ansys HFSS.

antennas have been widely studied, both theoretically and experimentally, in the open literature and have been shown to offer significant performance gains in multi-antenna systems by increasing channel capacity and enhancing robustness [9–11].

In this work, we provide a simulation-based analysis for implementing antenna reconfigurability in mmWave 5G communication. We first present a pattern reconfigurable cylindrical conformal antenna inspired by our previous work in [12]. This conformal antenna utilizes a 4×16 planar array, which is wrapped around a cylindrical supporting structure to form a cylindrical-shaped antenna. It achieves full 360° beam scanning in the azimuth plane using eight discrete directional beams, each produced by a 4×2 subarray. Its conformal design makes the antenna compact, significantly reducing the size of the electronic system. The antenna uses a single-port reconfigurable feeding network as the switching mechanism, requiring only a single RF chain, which reduces both hardware complexity and cost.

For the state-selection optimization process, we address the problem of reconfigurable antenna state selection in a single-user, single-RF chain mmWave communication system (where only one antenna state can transmit at a time [13]) by performing a simulation-based coverage analysis using a ray tracing simulator (Wireless InSite). This ray tracing software allows us to model various wireless channels and environmental conditions. To fully realize the potential benefits of reconfigurable antennas, selecting the optimal antenna state for communication is critical. Our simulation modeled a user

TABLE I: Cylindrical conformal antenna simulation results

State	Beam angle (°)	Gain (dBi)	HPBW (°)	Bandwidth (GHz)
State 1	170	8.9	29.57	1.15
State 2	220	7.4	32.88	0.95
State 3	260	7.6	34.42	0.83
State 4	310	8.7	32.71	0.99
State 5	350	8.9	28.81	0.99
State 6	40	8.76	41.64	0.92
State 7	80	8.6	34.91	1.04
State 8	120	9.4	41.97	0.72
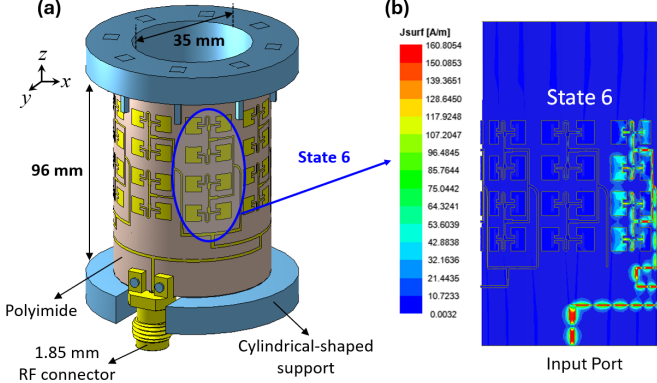
Fig. 2: (a) Simulation model of cylindrical conformal antenna. (b) Current distribution state 6.

Fig. 3: Cylindrical conformal antenna simulation results: (a) 3D and (b) 2D radiation patterns in the azimuth plane. (c) reflection coefficients (S_{11}) for all eight states at 28 GHz.

moving along a circular trajectory at a constant velocity. We evaluated the received power across different antenna states at each user position and identified the optimal state using a low-complexity beam selection algorithm, Adaptive Pursuit [14]. This algorithm efficiently leverages the sparse nature of mmWave channels and is well-suited for real-time 5G applications due to its rapid convergence. We also compared the performance of the Adaptive Pursuit algorithm against a random selection strategy and the ϵ-greedy policy.

II. ANTENNA DESIGN

Fig. 1 illustrates the geometry of the 4×16 planar array employed in the design of the cylindrical conformal antenna. This array consists of eight cascaded 4×2 subarrays, each composed of inset-fed patch antennas serving as the radiating elements. The inset-fed design was chosen to optimize return loss and simplify fabrication. The element spacing is set to $\lambda/2$, where λ represents the wavelength at 28 GHz. The radiating antenna elements are fed by a single-port corporate feeding network composed of 75Ω feeding lines, with the input feeding line having an impedance of 50Ω to ensure equal and in-phase excitation across all elements. To achieve in-phase excitation between adjacent elements oriented in opposite directions, as shown in Fig. 1, a passive $180°$ phase delay line is introduced at the T-junction within each 4×2 subarray. This phase shift is implemented by meandering the length of one of the feeding lines leading to the element. We designed and optimized the geometric parameters of the array antenna in Ansys HFSS to achieve optimal performance at 28 GHz, focusing on far-field radiation patterns and reflection coefficients ($|S_{11}|$). The overall dimensions of the antenna are 96 mm in length, 50 mm in height, and 0.29 mm in thickness, making it more practical for integration into space-constrained devices.
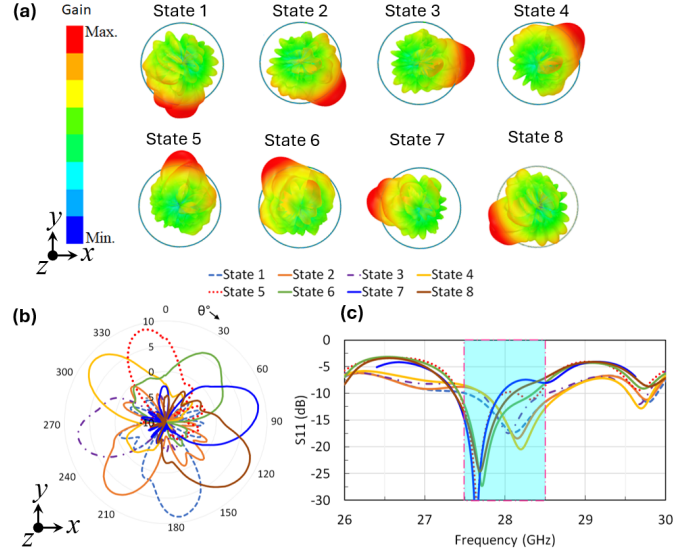
A. Conformal design

In the full-wave simulation, the conformal antenna, shown in Fig. 2(a), was designed by wrapping the 4×16 planar array (Fig. 1) around a cylindrical supporting structure to achieve a cylindrical shape. For this design, a polyimide dielectric substrate ($\varepsilon_r = 3.5$) was chosen due to its excellent conformability to non-planar surfaces and low dielectric loss ($tan(\sigma)$ = 0.006 at 20GHz). The antenna's extremely thin profile aids in maintaining conformity. We optimized the performance of the cylindrical conformal antenna, and a summary of key performance metrics, including gain, beam angle, half-power beamwidth (HPBW), and impedance bandwidth (at 28 GHz) for all eight operating states is provided in Table I.

B. Reconfigurability and switching mechanism

The pattern reconfigurability is achieved by electrically switching the beams of the eight 4×2 subarrays. This switching mechanism is implemented by integrating PIN diodes into the feed network, modeled as lumped RLC boundaries in the simulation. The PIN diodes are placed at each corporate feed junction (see Fig. 1), allowing dynamic control of the current flow as RF signals travel from the input port to the antenna elements, thus controlling which antenna state is activated, as shown in Fig. 2(b). The cylindrical conformal antenna design provides full $360°$ azimuthal coverage with eight distinct beam states, as demonstrated by the 3D and 2D radiation patterns in Fig. 3(a) and (b), respectively. The corresponding reflection coefficients ($|S_{11}|$) are shown in Fig. 3(c). It is important to note that the simulation did not account for the overall dimensions and material of the PIN diodes. Thus, the performance of the conformal antenna could be influenced by the packaging material of the PIN diodes during actual measurements.
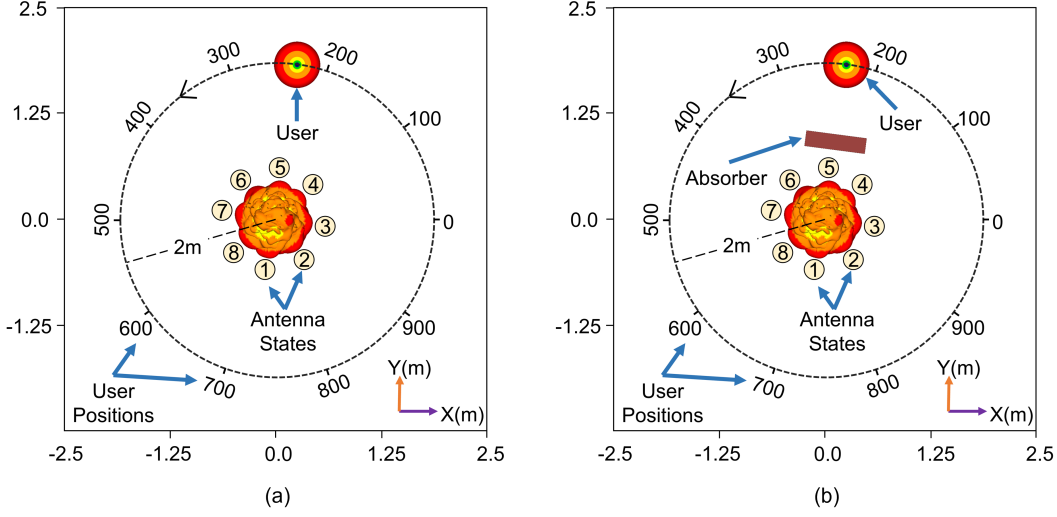
Fig. 4: Top view of the mmWave conformal antenna and the user in ray tracing simulation for a) LoS communication, and b) Non-LoS communication in the presence of an absorber. The user is moving in counter clockwise direction starting at x = 2, y = 0.

III. RAY TRACING SIMULATION

A. Simulating a Moving User

We simulated an indoor wireless environment using Wireless InSite ray tracing simulation software. The environment was modeled as a 5m × 5m × 5m room constructed from concrete. The mmWave cylindrical conformal antenna radiation beams, as simulated in Ansys HFSS, were imported into the ray tracing software and positioned at the center of the XY plane, 1m above the floor. This setup enabled the representation of 360° azimuthal beam scanning. To assess the performance of each antenna state with a mobile user, we simulated a user moving in a circular trajectory 2m away from the antenna at a constant velocity, as illustrated in Fig. 4. Since Wireless InSite does not natively support moving objects, we employed a post-processing technique to simulate the user's motion. This involved defining the user's trajectory and placing 1,000 omnidirectional antennas at fixed intervals along the path, each located 1m above the floor. For each position along the trajectory, we collected the received power levels, effectively capturing the dynamic changes in received power as the user moved through different locations. We also simulated two distinct scenarios for the moving user:

a) Line-of-sight (LoS) Communication: In this scenario (Fig. 4(a)), there are no obstacles between the antennas and the moving user, ensuring a consistent LoS path. This represents an ideal condition where communication is unobstructed, serving as a baseline for evaluating the antenna's state-selection performance in a perfect environment. Fig. 5(a) shows the received power levels of the moving user at different positions for all the antenna states. As expected, the power level is highest when the user is directly in front of an antenna, where a clear LoS communication path is present.

b) Communication in the Presence of Obstruction: In this scenario, we introduced a perfect absorber to block the LoS path between antenna state 5 and the user. The absorber is strategically placed at a specific location (Fig. 4(b)) to

effectively prevent any signal from state 5 from reaching the user via the LoS path. While the signal from state 5 may still reach the user via multipath reflections, as shown in Fig. 5(b), the power level of these reflected components is negligible compared to the LoS conditions observed in Fig. 5(a). Fig. 5(b) highlights the impact of the absorber on received power at various user locations. The received power from state 5 drops significantly due to the blockage, while locations with an unobstructed LoS path continue to experience high power levels. We collected received power data at each user location for all antenna states, both with and without the absorber. This data was subsequently used to post-process and verify the state selection algorithm, as well as to estimate the signal-to-noise ratio (SNR) performance under these two distinct scenarios with a mobile user. We assumed a communication channel modeled with additive white Gaussian noise (AWGN) with a channel bandwidth of 100 MHz for the SNR calculation. Accounting for the thermal noise power at room temperature (-174 dBm), noise power for 100 MHz of bandwidth (80 dBm), and a receiver noise figure of 3 dB, the effective noise power of the AWGN channel considered is -91 dBm.

It should be noted that the received power due to state 6 in Fig. 5 is significantly lower than that of the other states. This is because the radiated pattern for state 6, when imported into the ray-tracing simulation software, was somewhat distorted. This distortion resulted in a reduction of gain in the main lobe and consequently a lower received power level.

B. Antenna State Selection

For antenna state selection strategies, we investigate three different algorithms, described as follows:

- **Random State Selection:** This strategy naively selects any one of the antenna states with equal probability.
- **ϵ-greedy Algorithm:** This is a simple yet effective method to balance exploration and exploitation in reinforcement learning and multi-armed bandit problems. The
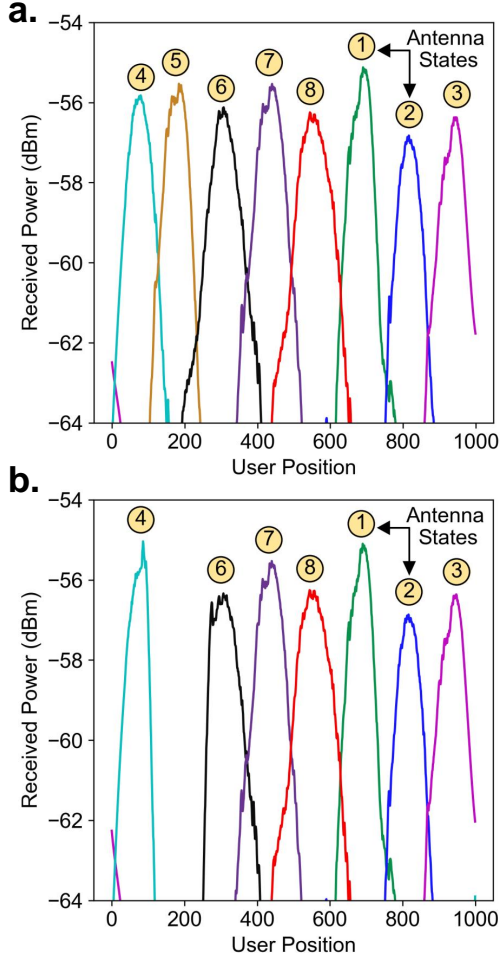
Fig. 5: Received power (smoothed) at different user locations (a) without, and (b) with blockage. When the user is directly in front of antenna 5, the absorber blocks the LoS path between antenna 5 and the user. The received power at antenna 5 drops drastically.

algorithm selects actions (in this case, the states of the antenna) based on two probabilities: 1) with probability ϵ, it chooses a random state, and 2) with probability $1 - \epsilon$, it selects the state yielding the maximum expected reward. The random state selection is referred to as exploration, while the algorithm performs exploitation by selecting the state with the highest estimated reward. Typically, the parameter ϵ is set to a low value to allow exploration of new states, which also implies a high exploitation rate for the best-known states. Over time, this method converges to the highest reward-yielding states.

- **Adaptive Pursuit (AP) Algorithm:** For real-time state selection, it is desirable to use a rapidly converging algorithm that adapts to dynamic environments and has low computational complexity. We adopted the machine-learning-based Adaptive Pursuit algorithm, which provides both flexibility and efficiency [15]. Given $\mathbf{K}$ possible states to choose from, the Adaptive Pursuit algorithm tracks two $\mathbf{K}$-length vectors: (a) the expected rewards vector $\bar{\mathbf{Q}}$, which stores each antenna state's expected reward (in this simulation, the received power), and (b)

TABLE II: Algorithms and Hyperparameters

Algorithm	Hyperparameters
Adaptive Pursuit	Learning rate of the expected reward vector: $\alpha = 0.25$, Learning rate of the probability vector: $\beta = 0.1$, Maximum probability of a state being selected: $P_{max} = 0.79, 0.86, 0.93$ Minimum probability of a state being selected: $P_{min} = 0.03, 0.02, 0.01$
ϵ-greedy	Exploration rate: $\epsilon = 0.05, 0.1, 0.15$ Exploration decay rate: 0.05 every 100 iteration
Random Selection	Equal probability of all the states being selected

the probability vector $\bar{\mathbf{P}}$, which stores the probability of each antenna state being selected. Each element of vector $\bar{\mathbf{P}}$ is bounded by $P_{\min}$ and $P_{\max} = 1 - (K - 1)P_{\min}$, and the individual probabilities in $\bar{\mathbf{P}}$ must sum to 1 ($\sum_{i=1}^{K} P_i = 1$). The vectors $\bar{\mathbf{Q}}$ and $\bar{\mathbf{P}}$ are updated using learning rates $\alpha \in (0, 1]$ and $\beta \in (0, 1]$ respectively, according to the following update rules:

$$\bar{Q}_i = (1 - \alpha)\bar{Q}_i + \alpha R_i$$

$$\bar{P}_i = \begin{cases} \bar{P}_i + \beta(P_{\max} - P_i), & \text{if } i = i^* \\ \bar{P}_i + \beta(P_{\min} - P_i), & \text{otherwise} \end{cases} \quad (1)$$

where R_i is the reward of state i and i^* is the state with maximum reward. A more detailed explanation of the Adaptive Pursuit algorithm is described in the following algorithm:

Algorithm 1 Adaptive Pursuit (AP) Algorithm

1: Initialization
2: $P \leftarrow 1/K$
3: $Q \leftarrow 0$
4: **while** True **do**
5:     Select state with probability distribution P
6:     Update expected reward for selected state i^*:
7:     $Q_{i^*} \leftarrow (1 - \alpha)Q_{i^*} + \alpha R_{i^*}$
8:     Update probability vector P:
9:     $P_i \leftarrow P_i + \beta(P_{\max} - P_i)$, if $i = i^*$
10:     $P_i \leftarrow P_i + \beta(P_{\min} - P_i)$, else
11: **end while**

The hyperparameters and their values used in the algorithms we investigate are presented in Table. II.

IV. RESULTS AND DISCUSSION

The selected states of the user as they move along the circular trajectory are depicted in Fig. 6, comparing the Adaptive Pursuit, ϵ-greedy, and random selection algorithms, presented in three columns. The first column represents the selected states using the Adaptive Pursuit algorithm, the second column illustrates the results for the ϵ-greedy algorithm, and the third column shows the randomly selected states. In each column, the top row reflects the state selection under LoS conditions—without any absorber, while the bottom row presents the state selection in non-LoS conditions (with an absorber). Fig. 6 (a) and (b) illustrate step-like patches representing the LoS communication with the selected antenna state for the LoS condition. Both the Adaptive Pursuit and ϵ-greedy algorithms
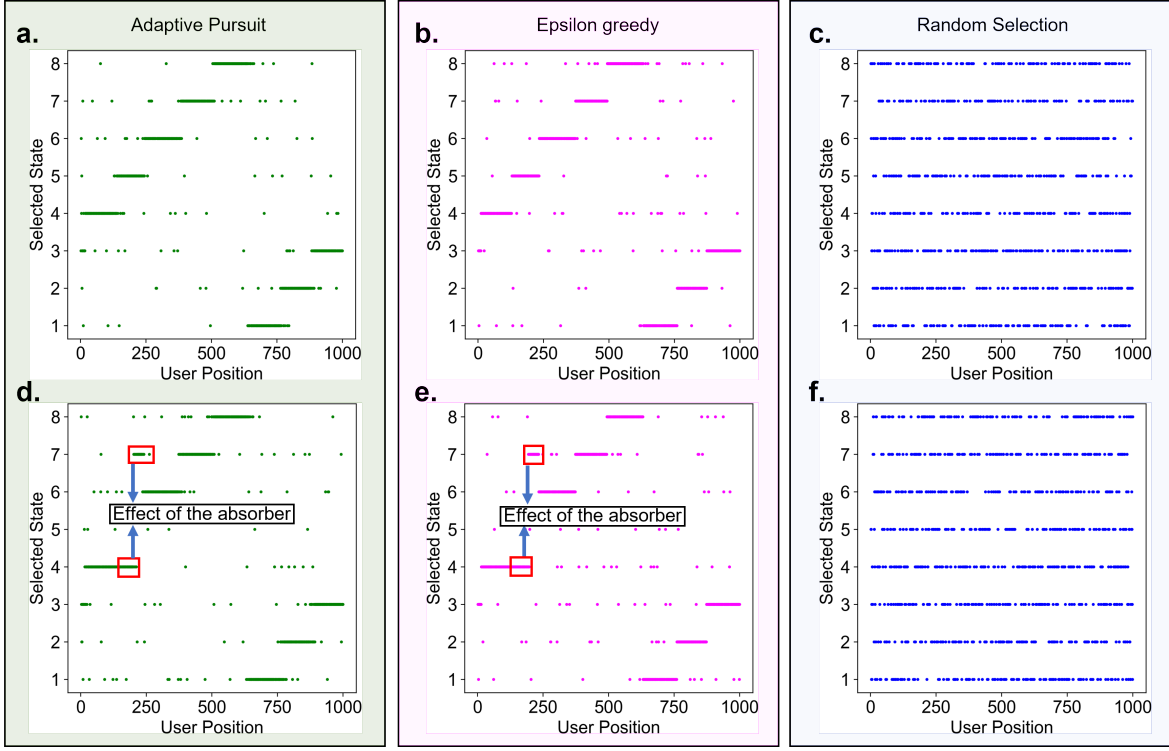
Fig. 6: Selected states by (a) Adaptive Pursuit, (b) ϵ-greedy, and (c) random selection algorithms when there is no absorber. With the introduction of the absorber, state 5 gets blocked and the plots (d), (e), and (f) represent the selected states for Adaptive Pursuit, ϵ-greedy, and random selection algorithms, respectively.
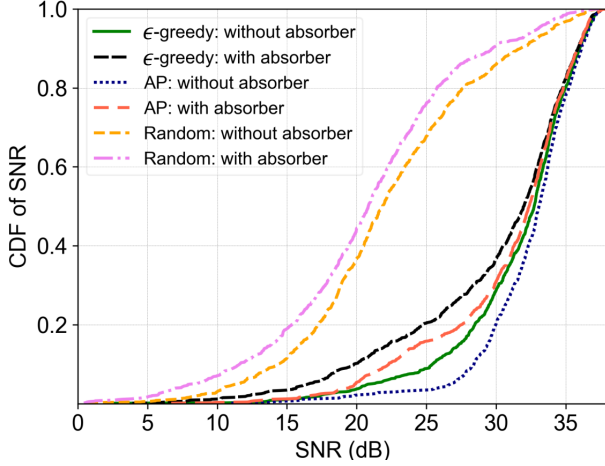

Fig. 7: Cumulative distribution function (CDF) of SNR for the Adaptive Pursuit (P_{max} = 0.93) and ϵ-greedy ($\epsilon = 0.05$) algorithms with and without absorbers.
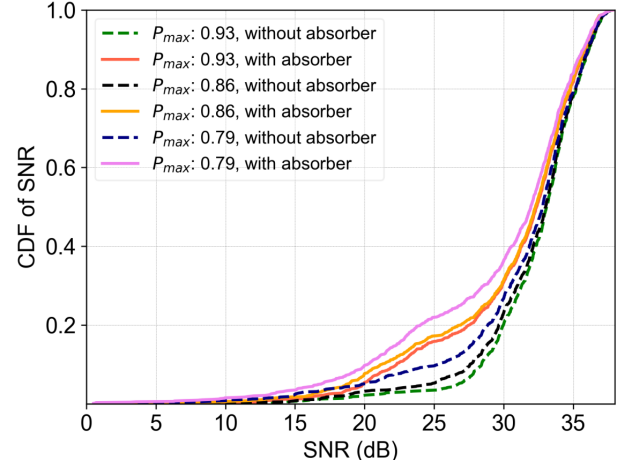
Fig. 8: Cumulative distribution function (CDF) of SNR for the Adaptive Pursuit algorithm for different values of P_{max}.

exhibit rapid convergence as the user changes position. Due to the user's uniform velocity, the selected states (patches) are almost of the same width. However, for the random selection case, there is no discernible or predictable pattern.

Around position 200 of the user's trajectory, we introduced a perfect absorber to break the LoS path between the user and state 5. As a result, both the Adaptive Pursuit and ϵ-greedy algorithms rapidly converged to select state 4 and state 7. State 5 is not selected for the entire duration when the LoS link is broken. State 4, being adjacent to state 5, gets selected due to the blocked LoS path. However, state 7 accumulates higher

expected rewards than state 6, the other adjacent antenna state, because state 6 offers lower received power. Therefore, both Adaptive Pursuit and ϵ-greedy converge on state 7. As expected, the introduction of the absorber shows no significant impact on the random selection process (Fig. 6(f)). Moreover, both the Adaptive Pursuit and ϵ-greedy algorithms rapidly converged to the optimized states under both LoS and non-LoS communication conditions. The presence of an absorber in the scene degrades the signal quality and deteriorates the SNR. Fig. 7 shows the cumulative probability distribution (CDF) of SNR for the Adaptive Pursuit, ϵ-greedy, and random selection algorithms with and without the absorber. The Adaptive
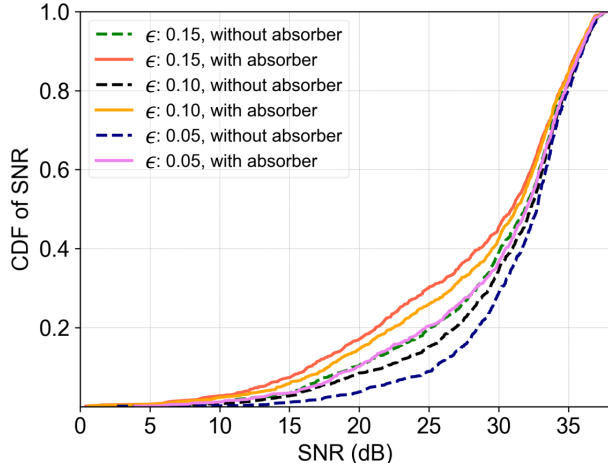
Fig. 9: Cumulative distribution function (CDF) of SNR for the ϵ-greedy algorithm for different values of ϵ.

Pursuit algorithm achieves the highest SNR probability in both scenarios, with and without the absorber. As expected, the random selection algorithm shows the lowest SNR probability. We also investigated different parameter values for the Adaptive Pursuit and ϵ-greedy algorithms (see Fig. 8 and Fig. 9). For the Adaptive Pursuit algorithm, a $P_{max} = 0.93$ yields the highest SNR performance, while for the ϵ-greedy algorithm, an $\epsilon = 0.05$ provides the best SNR. Thus, the simulation and results demonstrate that deploying a reconfigurable mmWave antenna with adaptive state selection strategies can significantly enhance signal quality, improve SNR, and increase communication reliability in dynamic environments by quickly adapting to varying conditions. Furthermore, the reconfigurable mmWave antenna can enhance low-latency beamforming, which is key for the practical deployment of mmWave hardware platforms as discussed in [16].

V. Conclusion

We presented a $360°$ beam-steerable mmWave cylindrical conformal antenna designed for 5G indoor coverage. The antenna's reconfigurability allows us to dynamically change its radiation characteristics using eight discrete directional beams (states). To identify or predict the optimal antenna state for maintaining a reasonable SNR in dynamic mmWave environments, we employed a low-complexity, rapid-convergence, ML-based state selection algorithm. This algorithm was validated by simulating a single-user, single RF chain 5G communication system (where only one antenna state transmits at a time) using ray tracing software and comparing the results to other algorithms in the literature.

In the future, we plan to prototype and experimentally demonstrate a fully functional beam-steerable cylindrical conformal antenna with integrated RF switch control circuitry to dynamically control antenna states. Also, we aim to use the antenna for wireless indoor localization and integrate it with our mmWave Software Defined Radio Network Testbed [17, 18].

REFERENCES

[1] T. S. Rappaport, Y. Xing, G. R. MacCartney, A. F. Molisch, E. Mellios, and J. Zhang, "Overview of millimeter wave communications for fifth-generation (5G) wireless networks—with a focus on propagation models," *IEEE Transactions on Antennas and Propagation*, vol. 65, no. 12, pp. 6213–6230, 2017.

[2] Z. Pi and F. Khan, "An introduction to millimeter-wave mobile broadband systems," *IEEE Communications Magazine*, vol. 49, no. 6, pp. 101–107, 2011.

[3] T. Rappaport, R. Heath, R. Daniels, and J. Murdock, *Millimeter Wave Wireless Communications*. Prentice Hall, 2014.

[4] I. Mallioras, T. V. Yioultsis, N. V. Kantartzis, P. I. Lazaridis, and Z. D. Zaharis, "Enhancing adaptive beamforming in 3-D space through self-improving neural network techniques," *IEEE Open Journal of the Communications Society*, vol. 5, pp. 1340–1357, 2024.

[5] A. M. Montaser, "Machine learning based design of pattern reconfigurable antenna," *IEEE Access*, vol. 11, pp. 33 121–33 133, 2023.

[6] H. Pablo Zapata Cano, Z. D. Zaharis, T. V. Yioultsis, N. V. Kantartzis, and P. I. Lazaridis, "Pattern reconfigurable antennas at millimeter-wave frequencies: A comprehensive survey," *IEEE Access*, vol. 10, pp. 83 029–83 042, 2022.

[7] B. R. Jackson, "2D direction of arrival estimation using uniform circular arrays with radiation pattern reconfigurable antennas," *IEEE Access*, vol. 10, pp. 11 909–11 923, 2022.

[8] M. S. Hossain, M. A. S. Tajin, and K. R. Dandekar, "UHF RFID tag localization using pattern reconfigurable reader antenna," in *2022 IEEE 22nd Annual Wireless and Microwave Technology Conference (WAMICON)*, 2022, pp. 1–4.

[9] J. D. Boerman and J. T. Bernhard, "Performance study of pattern reconfigurable antennas in MIMO communication systems," *IEEE Transactions on Antennas and Propagation*, vol. 56, no. 1, pp. 231–236, 2008.

[10] D. Piazza, N. J. Kirsch, A. Forenza, R. W. Heath, and K. R. Dandekar, "Design and evaluation of a reconfigurable antenna array for MIMO systems," *IEEE Transactions on Antennas and Propagation*, vol. 56, no. 3, pp. 869–881, 2008.

[11] S. F. Jilani, B. Greinke, Y. Hao, and A. Alomainy, "Flexible millimetre-wave frequency reconfigurable antenna for wearable applications in 5G networks," in *2016 URSI International Symposium on Electromagnetic Theory (EMTS)*, 2016, pp. 846–848.

[12] A. Stroh, M. Sigda, K. Carbone, D. Baun, M. A. S. Tajin, O. Bshara, V. Pano, and K. R. Dandekar, "A pattern reconfigurable conformal mmwave antenna for 5G applications," in *2021 IEEE International Symposium on Antennas and Propagation and USNC-URSI Radio Science Meeting (APS/URSI)*, 2021, pp. 1059–1060.

[13] M. D. S. Huque, C. Surekha, S. P. K. Reddy, and V. Yadav, "The differentiation between MIMO with other antennas," *CoRR*, vol. abs/1207.0665, 2012. [Online]. Available: http://arxiv.org/abs/1207.0665

[14] S. Wolfe, S. Begashaw, Y. Liu, and K. R. Dandekar, "Adaptive link optimization for 802.11 UAV uplink using a reconfigurable antenna," in *IEEE Military Communications Conference (MILCOM)*, 2018, pp. 1–6.

[15] X. R. Rey, G. Mainland, and K. Dandekar, "Real-time online learning for pattern reconfigurable antenna state selection," in *2020 7th NAFOSTED Conference on Information and Computer Science (NICS)*, 2020, pp. 13–18.

[16] O. Bshara, V. Pano, M. A. S. Tajin, and K. R. Dandekar, "Millimetre wave coarse beamforming using outband sub-6 GHz reconfigurable antennas," *IET Communications*, vol. 15, no. 19, pp. 2448–2460, 2021. [Online]. Available: https://ietresearch.onlinelibrary.wiley.com/doi/abs/10.1049/cmu2.12285

[17] K. R. Dandekar, S. Begashaw, M. Jacovic, A. Lackpour, I. Rasheed, X. R. Rey, C. Sahin, S. Shaher, and G. Mainland, "Grid software defined radio network testbed for hybrid measurement and emulation," in *2019 16th Annual IEEE International Conference on Sensing, Communication, and Networking (SECON)*, 2019, pp. 1–9.

[18] M. Jacovic, X. R. Rey, G. Mainland, and K. R. Dandekar, "Mitigating RF jamming attacks at the physical layer with machine learning," *IET communications*, vol. 17, no. 1, pp. 12–28, 2023.